Journal of Sound and Vibration 619 (2025) 119370

Contents lists available at ScienceDirect

Journal of Sound and Vibration

journal homepage: www.elsevier.com/locate/jsvi

Data-driven collaborative optimal design of acoustic black hole in panel flutter suppression

Zhuogeng Zhang [a], Xiaodong Wang [b], Hongli Ji [a,*], Jinhao Qiu [a], Li Cheng [c]

[a] College of Aerospace, Nanjing University of Aeronautics and Astronautics, Nanjing 210016, China
[b] Inner Mongolia Power Machineries Institute, Hohhot 010010, China
[c] Department of Mechanical Engineering, Hong Kong Polytechnic University, Hung Hom, Kowloon 99907, Hong Kong

ARTICLE INFO

Keywords:
Panel flutter
Acoustic black hole
Data-driven collaborative optimization
Flutter suppression

ABSTRACT

This study delves into the flutter critical boundary of panel with an Acoustic Black Hole (ABH) and its optimization and proposed an innovative optimization framework that combines a data-driven approach with physical mechanisms. At the panel-ABH interface, an improved coupled model was established by considering both the z-direction displacements and the rotations around the x and y axes. Leveraging the modal condensation theory, a comprehensive analysis is performed on how various modal parameters intricately interact to influence the aeroelastic response. To achieve larger flutter boundary, a hybrid surrogate model is developed to effectively capture the relationships between multiple inputs and output objectives. A closed-loop verification mechanism linking the surrogate model's prediction errors and finite element solutions is established, requiring only 225 model simulations to obtain an optimal design. The results show the optimized ABH can enhance the panel's flutter boundary by up to 29.4 %, nearly tripling the initial effect, fully demonstrating the superiority of the optimization. Moreover, the analysis of ABH's effective modal distribution and effective modal mass were conducted, thereby elucidating the mapping relationship between physical mechanisms and optimization performance, providing a theoretical basis for the superiority of the proposed method.

1. Introduction

Panel flutter is a typical aeroelastic instability that can lead to fatigue damage or catastrophic failure in high-speed aerospace structures [1–3]. Understanding the mechanism of panel flutter and developing effective suppression strategies are therefore of great interest. Over the past decades, a wide range of passive and active control approaches have been proposed by researchers. Passive methods include linear tuned mass dampers, nonlinear energy sinks, and so on [4–7], while active strategies employ piezoelectric actuators or shape memory alloys to dynamically adjust structural properties [8–11]. These methods have achieved varying degrees of success and provide diverse options for flutter control.

In recent years, Acoustic Black Hole (ABH) structures have attracted considerable attention as a novel passive control technique, due to their unique wave manipulation and energy dissipation characteristics [12–14]. Compared to conventional control devices, ABHs offer advantages such as light weight and broadband damping. A variety of ABH designs, including embedded and add-on configurations, one-dimensional tapers, circular and eccentric profiles, and swirl-shaped geometries, have been explored for their

* Corresponding author.
E-mail addresses: jihongli@nuaa.edu.cn, 625135215@qq.com (H. Ji).

https://doi.org/10.1016/j.jsv.2025.119370
Received 24 April 2025; Received in revised form 28 July 2025; Accepted 4 August 2025
Available online 6 August 2025

effectiveness in vibration and acoustic suppression [15–18].

Given their capacity to concentrate and dissipate structural vibration energy, ABHs have also shown promise in addressing aeroelastic instabilities such as panel flutter. This extension of ABH application into the fluid-structure interaction domain has led to several pioneering studies. Zhang et al [19] employed commercial finite element software coupled with a fluid-structure interaction simulation framework to demonstrate that ABHs can transfer and dissipate flutter-induced energy similarly to linear energy sinks, thereby effectively suppressing panel flutter. Moreover, Zhang et al [20] proposed a coupled aeroelastic analysis approach integrating the finite element method with dynamic analysis, and introduced a modal condensation theory to enhance computational efficiency. These efforts laid a solid theoretical foundation for applying ABHs in flutter control and broadened their application beyond traditional structural damping scenarios.

Despite these advances, ABH-based flutter suppression remains a highly parameter-sensitive problem due to the complex interplay between ABH geometry, modal behavior, and aeroelastic response. As indicated in Ref [20], key modal parameters, including natural frequencies, damping ratios, and modal participation factors, play a crucial role in determining the ABH's effectiveness, and these are strongly influenced by the ABH's geometric design. In addition, the installation location significantly affects the flutter boundary. Notably, our recent investigations revealed that certain ABH-induced modes, particularly those involving rotational degrees of freedom, which were previously excluded in our modal condensation-based aeroelastic model, can significantly influence flutter behavior, even when their effective mass and damping ratios are relatively small. This finding underscores the importance of incorporating a wider range of modal interactions in simplified coupled analyses.

To this end, we propose a collaborative optimization method that simultaneously considers both ABH geometric parameters and installation position. The goal is to identify optimal configurations that achieve enhanced flutter suppression performance [21,22]. However, this optimization problem is computationally demanding. On one hand, high-fidelity simulations under supersonic conditions with finely meshed ABH structures incur significant computational costs. On the other hand, although the numerical framework developed in Ref [20] improves efficiency via modal parameter-based analysis, generating the required modal data through finite element analysis remains time-consuming. These challenges hinder the practical deployment of ABH-based optimization strategies.

To overcome this issue, data-driven approaches have emerged as promising tools for high-dimensional structural optimization. For instance, Bessa et al.[23] combined Gaussian regression with a data-driven framework to design deployable shells. Liu et al.[24] used deep learning for multistable metamaterial beam optimization. Wilt et al.[25] developed machine learning models to predict auxetic material behavior. Inspired by these advances, we adopt a similar data-driven method for the optimization of ABH geometry and layout for flutter control.

In this study, a data-driven collaborative optimization framework is proposed to systematically investigate the effect of ABH structural geometry and installation position on panel flutter suppression. First, an improved aeroelastic model is developed that incorporates both translational and rotational degrees of freedom in the interaction force. Using modal condensation, we analyze the influence of ABH-induced modes on flutter behavior. To accelerate the optimization process, a surrogate modeling strategy combining a genetic algorithm optimized backpropagation neural network (GA-BP) and a genetic algorithm (GA) is introduced. This framework requires only 225 finite element simulations to effectively solve the optimization problem. The optimized ABH design demonstrates significant improvements in flutter suppression. Finally, the physical mechanisms underlying these improvements are analyzed, with special attention paid to the role of the rotational degrees of freedom in the interaction force.

The remainder of the paper is organized as follows. Section 2 introduces the coupled aeroelastic model and discusses the influence of ABH modal characteristics on flutter behavior. Section 3 presents the data-driven optimization framework and outlines the GA-BP based optimization strategy. Section 4 evaluates the optimized ABH design in terms of flutter suppression performance and reveals the underlying mechanisms. Section 5 concludes the study with key findings and future directions.

2. Modelling, calculation, and analysis

2.1. Reduced model for panel with ABH

The aeroelastic model of four-side simply supported panel with ABH is shown in Fig. 1. The length, width and thickness of the panel

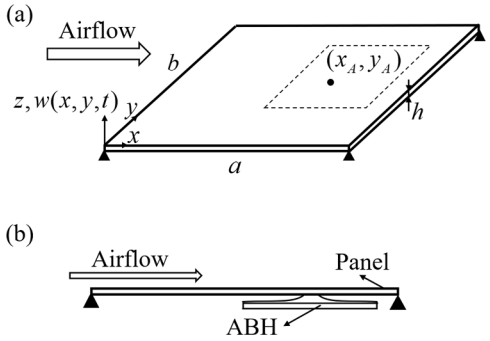

Fig. 1. Schematic of a panel with ABH structure. (a) 3-D view, (b) 2-D view.

are a, b, and h respectively. The one side of panel is exposed to airflow, while the ABH is attached to the other side. The installation position coordinates are marked as (x_A, y_A).

By integrating von Karman's large deformation theory, aerodynamic loads p_a, in-plane external loads $p_x^{(a)}$, $p_y^{(a)}$, and forces f_{ABH} exerted on the panel by ABH, the aeroelastic equations of panel with ABH can be established. In our previous work [20], a comprehensive derivation and detailed description of these equations for solving aeroelastic response of panel with ABH were presented, along with explicit definitions of each symbol within these equations. The dimensionless equations of panel can be expressed in the following form:

$$\begin{cases} \dfrac{\partial^4 \overline{w}}{\partial \xi^4} + 2s_b^2 \dfrac{\partial^4 \overline{w}}{\partial \xi^2 \partial \eta^2} + s_b^4 \dfrac{\partial^4 \overline{w}}{\partial \eta^4} = s_b^2 \left(\dfrac{\partial^2 \overline{\varphi}}{\partial \eta^2} \cdot \dfrac{\partial^2 \overline{w}}{\partial \xi^2} - 2 \dfrac{\partial^2 \overline{\varphi}}{\partial \xi \partial \eta} \cdot \dfrac{\partial^2 \overline{w}}{\partial \xi \partial \eta} + \dfrac{\partial^2 \overline{\varphi}}{\partial \xi^2} \cdot \dfrac{\partial^2 \overline{w}}{\partial \eta^2} \right) \\ + \overline{p}_x^{(a)} \dfrac{\partial^2 \overline{w}}{\partial \xi^2} + \overline{p}_y^{(a)} s_b^2 \dfrac{\partial^2 \overline{w}}{\partial \eta^2} - \dfrac{\partial^2 \overline{w}}{\partial \tau^2} + \overline{p}_a + \overline{f}_{ABH} \\ \dfrac{\partial^4 \overline{\varphi}}{\partial \xi^4} + 2s_b^2 \dfrac{\partial^4 \overline{\varphi}}{\partial \xi^2 \partial \eta^2} + s_b^4 \dfrac{\partial^4 \overline{\varphi}}{\partial \eta^4} = 12(1-\nu^2) \left[\left(\dfrac{\partial^2 \overline{w}}{\partial \xi \partial \eta} \right)^2 - \dfrac{\partial^2 \overline{w}}{\partial \xi^2} \cdot \dfrac{\partial^2 \overline{w}}{\partial \eta^2} \right] \end{cases} \tag{1}$$

where the dimensionless variables and parameters are defined as follows:

$$\begin{aligned} &\overline{w} = \frac{w}{h}, \quad \xi = \frac{x}{a}, \quad \eta = \frac{y}{b}, \quad \tau = t\left(\frac{D}{\rho h a^4}\right)^{1/2}, \quad \overline{\varphi} = \frac{h}{D}\varphi, \\ &\beta = \sqrt{Ma^2 - 1}, \quad s_b = \frac{a}{b}, \quad \lambda = \frac{2pa^3}{\beta D}, \quad \overline{p}_{x(y)}^{(a)} = \frac{p_{x(y)}^{(a)} a^2}{D}, \quad \overline{f}_{\mathrm{ABH}} = \frac{a^3}{Dbh} f_{\mathrm{ABH}} \\ &\overline{p}_a = -\left(\lambda \frac{\partial \overline{w}}{\partial \xi} + \sqrt{\lambda R_M}\ \frac{\partial \overline{w}}{\partial \tau} \right), \quad R_M = \frac{\mu}{\beta}, \quad \mu = \frac{\rho_a a}{\rho h} \end{aligned} \tag{2}$$

in which w is lateral displacement and φ is Airy stress potential function. $D = Eh^3/12(1-\nu^2)$ denotes the bending stiffness of panel, E is Young's modulus, ν is Poisson's ratio, ρ represents panel's density. λ is dimensionless form of dynamic pressure which is used to measure the magnitude of the inflow. $p = \rho_a V_\infty^2/2$ is dynamic pressure. ρ_a and V_∞ are the air density and the far field airflow velocity, respectively. The aerodynamic load $\overline{p}_a$, based on the first-order piston theory approximation [7], is a transient parameter that is closely related to the dynamic pressure and panel's displacement.

As introduced in the next section, the f_{ABH} includes effect of the concentrated out-of-plane force F_{ABH} and moment $M_{\mathrm{ABH}x}$ with respect to x and moment $M_{\mathrm{ABH}y}$ with respect to y generated by the translational and rotational motion of the ABH. When the coordinate of the installation point is denoted by (x_A, y_A), f_{ABH} can be expressed by

$$f_{ABH} = F_{ABH}\delta(x - x_A, y - y_A) + M_{ABHx}\delta'_y(x - x_A, y - y_A) + M_{ABHy}\delta'_x(x - x_A, y - y_A) \tag{3}$$

where $\delta(x, y)$ is a two-dimensional impulse function. δ'_x and δ'_y are the derivatives of the δ function with respect to x and y axes, respectively

Eqs. (1) and (2) were solved using Galerkin's method developed by Dowell [26]. For a simply supported panel with four edges, the response of panel is approximated using Galerkin's method and expressed as:

$$\overline{w}(\xi, \eta, \tau) = \sum_{n=1}^{M} q_n(\tau) \sin(n\pi\xi) \sin(\pi\eta) \tag{4}$$

where $q_n(\tau)$ is the coordinate corresponding to basis function $\sin(n\pi\xi)\sin(\pi\eta)$.

Following Galerkin's method we multiply the Eq. (1) by basis function $\sin(n\pi\xi)\sin(\pi\eta)$, $(n = 1, 2, \cdots, M)$ and integrate along the chord and spanwise directions of the panel for ξ and η in the interval $[0, 1]$. The result of ordinary differential equation about the coordinate $q_n(\tau)$ is obtained:

$$\begin{aligned} \frac{d^2 q_n}{d\tau^2} = &-q_n \pi^4 \left[n^2 + (a/b)^2 \right]^2 - \lambda \left\{ \sum_{m=1, m \neq n}^{M} \frac{2nm}{n^2 - m^2} [1 - (-1)^{n+m}] q_m + \sqrt{\frac{\mu}{Ma\lambda}}\ \frac{dq_n}{d\tau} \right\} \\ &- 3\pi^4 (1 - \upsilon^2) \left\{ \frac{q_n}{2} \left[n^2 A + (a/b)^2 B \right] + (a/b)^4 \left(C_n + D_n + \frac{E_n}{4} - \frac{F_n}{2} \right) \right\} - \overline{F}^*_{ABH,n} \\ &- \overline{p}_x^{(a)} \pi^2 n^2 q_n - \overline{p}_y^{(a)} \pi^2 (a/b)^2 q_n (n = 1, 2, \cdots, M) \end{aligned} \tag{5}$$

where $\overline{F}^*_{ABH,n}$ is the force corresponding to $q_n(\tau)$ generated by ABH and its expression contains the modal coordinates of the ABH, $A \sim F_n$ and constants are defined in Ref [20]. $\overline{F}^*_{ABH,n}$ is calculated from the following integration:

$$\overline{F}^{*}_{ABH,n} = 4\int_0^1\int_0^1 \bar{f}_{ABH}\sin(n\pi\xi)\sin(\pi\eta)d\xi d\eta \tag{6}$$

After substitution of Eq. (3) into $\bar{f}_{ABH}$ in Eq. (2) and then into Eq. (6), the force $\overline{F}^{*}_{ABH,n}$ can be expressed as

$$\begin{aligned}\overline{F}^{*}_{ABH,n} &= 4\overline{F}_{\mathrm{ABH}}\sin(n\pi\xi_A)\sin(\pi\eta_A)\\ &+4\pi\overline{M}_{\mathrm{ABHx}}\sin(n\pi\xi_A)\cos(\pi\eta_A) + 4n\pi\overline{M}_{\mathrm{ABHy}}\cos(n\pi\xi_A)\sin(\pi\eta_A)\end{aligned} \tag{7}$$

where $\overline{F}_{ABH} = \frac{a^3}{Dbh}F_{ABH}$, $\overline{M}_{\mathrm{ABHx}} = \frac{a^3}{Db^2h}M_{\mathrm{ABHx}}$, $\overline{M}_{\mathrm{ABHy}} = \frac{a^2}{Dbh}M_{\mathrm{ABHy}}$.

The ABH was discretized using Finite Element Method (FEM) and modal analysis was carried based on clamped boundary at the interface between ABH and panel. This ensures that at the contact points, the displacements on both sides of the installation interface remain equal, satisfying the displacement transmissibility. Therefore, when ABH is fixed on the panel at position (x_A, y_A), its displacement $\mathbf{w}_A$ is the sum of the elastic displacement of ABH and the rigid mode displacement induced by panel's displacement $w(x_A, y_A, t)$ at contact point.

In the former study, one translational rigid mode was taken into consideration in the approximation of ABH displacement, which expressed as [17]:

$$\mathbf{w}_A = \boldsymbol{\phi}_A\mathbf{q}_A + \mathbf{1}w(x_A, y_A, t) \tag{8}$$

where $\boldsymbol{\phi}_A = \{\boldsymbol{\phi}_1, \boldsymbol{\phi}_2, \cdots, \boldsymbol{\phi}_I\}$ is modal matrix of the ABH normalized with respect to the mass matrix, $\mathbf{q}_A$ is modal coordinate of ABH, and $\mathbf{1}$ is a vector with all components equal to 1. I is the total number of considered modes. It is easy to understand that $\mathbf{1}$ is modal vector of the translational mode. Substitution of the above displacement into FEM equation gives,

$$\mathbf{I}\ddot{\mathbf{q}}_A + \mathbf{C}\dot{\mathbf{q}}_A + \mathbf{K}\mathbf{q}_A = \mathbf{F} \tag{9}$$

where $\mathbf{F}$ is the force induced by vibration of panel and its expression contains the displacement $w(x_A,y_A,t)$, $\mathbf{C}$ is a matrix with diagonal elements as $2\omega_{Ai}\zeta_{Ai}$, $\mathbf{K}$ is a matrix with diagonal elements as ω^2_{Ai}. ω_A and ζ_A are the modal frequency and damping ratio of the ABH, respectively.

As introduced above, Eqs. (5) and (9) are the equations of motion of the panel and ABH, and they coupled through the terms of forces $\overline{F}^{*}_{ABH,n}$ and $\mathbf{F}$, constituting the reduced model of the coupled panel-ABH system.

2.2. Improved coupled model

The displacement $\mathbf{w}_A$ of ABH is closely related to three rigid modes, one translational, one rotational with respect to x axis and one rotational with respect to y axis. In the former study, only the translational was taken into consideration for simplicity. In this study, all the three rigids' modes are taken into consideration and the improved displacement's expression is:

$$\mathbf{w}_A = \boldsymbol{\phi}_A\mathbf{q}_A + \mathbf{1}w(x_A, y_A, t) + \mathbf{R}_x\theta_x(x_A, y_A, t) + \mathbf{R}_y\theta_y(x_A, y_A, t) \tag{10}$$

where $\mathbf{R}_x$ and $\mathbf{R}_y$ are rotational modal vectors, $\theta_x(x_A, y_A, t)$ and $\theta_y(x_A, y_A, t)$ are the rotational angles of the panel at (x_A,y_A), with respect to x and y axes, respectively. The components $\mathbf{R}_x$ and $\mathbf{R}_y$ are proportional to the distances of the corresponding node on the ABH structure to the x and y axes, respectively.

In contrast to the coupling model in the former study, the new coupling model not only consider the displacement of the ABH induced by the translational displacement of the panel along the z-axis, $w(x_A,y_A,t)$, but also the displacement resulting from rotations about the x and y axes, $\theta_x(x_A, y_A, t) = \partial w(x_A, y_A, t)/\partial y, \theta_y(x_A, y_A, t) = \partial w(x_A, y_A, t)/\partial x$, as shown in Eq. (10). As a result, the actual displacement of the ABH comprises four components: displacement determined by the elastic modes, z-axis displacement of the panel, and the displacement resulting from rotations about the x and y axes.

To derive the excitation force acting the ABH based on the new coupling model, the equation of motion of the ABH in modal space is expressed as

$$\mathbf{M}_A\ddot{\mathbf{w}}_A + \mathbf{C}_A\dot{\mathbf{w}}_A + \mathbf{K}_A\mathbf{w}_A = \boldsymbol{0}. \tag{11}$$

where the $\mathbf{M}_A$ is the mass matrices of ABH, $\mathbf{C}_A$ is the damping matrix and $\mathbf{K}_A$ is stiffness matrix of the ABH.

Substitution of Eq. (10) into (11) and multiplication of it by $\boldsymbol{\phi}_A^T$ from left give Eq. (9). The corresponding modal force $\mathbf{F}$ will be transformed into:

$$\mathbf{F} = -\boldsymbol{\phi}_A^T\mathbf{M}_A\mathbf{1}\ddot{w}(x_A, y_A, t) - \boldsymbol{\phi}_A^T\mathbf{M}_A\mathbf{R}_x\ddot{\theta}_x(x_A, y_A, t) - \boldsymbol{\phi}_A^T\mathbf{M}_A\mathbf{R}_y\ddot{\theta}_y(x_A, y_A, t) \tag{12}$$

where the $\boldsymbol{\phi}_A^T\mathbf{M}_A\mathbf{1}$, $\boldsymbol{\phi}_A^T\mathbf{M}_A\mathbf{R}_x$, and $\boldsymbol{\phi}_A^T\mathbf{M}_A\mathbf{R}_y$ are precisely the modal participation factors of the ABH structure in three directions as described in Ref [27], which will be discussed in detail later. The modal participation factors $\alpha_i^{(1)} = \boldsymbol{\phi}_{Ai}^T\mathbf{M}_A\mathbf{1}$, $\alpha_i^{(2)} = \boldsymbol{\phi}_{Ai}^T\mathbf{M}_A\mathbf{R}_x$ and $\alpha_i^{(3)} = \boldsymbol{\phi}_{Ai}^T\mathbf{M}_A\mathbf{R}_y$ $(i = 1, \cdots, I)$ will be calculated for considered modes of the ABH.

Next, the concentrated force F_{ABH} and the concentrated moments M_{ABHx} and M_{ABHy} in Eq. (3) need to be derived. They are induced

by the inertial force of the ABH, which can be expressed as $\mathbf{M}_A\ddot{\mathbf{w}}_A$ at all the nodes of the FEM model. Because $F_{\mathbf{ABH}}$ is the summation of all the components in $\mathbf{M}_A\ddot{\mathbf{w}}_A$, it can be expressed as

$$\begin{aligned} F_{ABH} &= -\mathbf{1}^T\mathbf{M}_A\ddot{\mathbf{w}}_A \\ &= -\mathbf{1}^T\mathbf{M}_A\boldsymbol{\phi}_A\ddot{\mathbf{q}}_A - \mathbf{1}^T\mathbf{M}_A\mathbf{1}\ddot{w}(x_A, y_A, t) \\ &\quad -\mathbf{1}^T\mathbf{M}_A\mathbf{R}_x\ddot{\theta}_x(x_A, y_A, t) - \mathbf{1}^T\mathbf{M}_A\mathbf{R}_y\ddot{\theta}_y(x_A, y_A, t) \end{aligned} \tag{13}$$

If the rigid modes $\mathbf{1}$, $\mathbf{R}_x$ and $\mathbf{R}_y$ are assumed to be orthogonal to each other with respect to the mode mass matrix $\mathbf{M}_A$, the above expression can be further simplified to

$$F_{ABH} = -\mathbf{1}^T\mathbf{M}_A\ddot{\mathbf{w}}_A = -\mathbf{1}^T\mathbf{M}_A\boldsymbol{\phi}_A\ddot{\mathbf{q}}_A - \mathbf{1}^T\mathbf{M}_A\mathbf{1}\ddot{w}(x_A, y_A, t) \tag{14}$$

Similarly, the moments M_{ABHx} is the summation of the components of $\mathbf{M}_A\ddot{\mathbf{w}}_A$ multiplied by the distance from the nodes to the x axis and the moments M_{ABHy} is the summation of the components of $\mathbf{M}_A\ddot{\mathbf{w}}_A$ multiplied by the distance from the nodes to the y axis. Therefore, they can be expressed in the following:

$$M_{ABHx} = -\mathbf{R}_x^T\mathbf{M}_A\ddot{\boldsymbol{w}}_A = -\mathbf{R}_x^T\mathbf{M}_A\boldsymbol{\phi}_A\ddot{\boldsymbol{q}}_A - \mathbf{R}_x^T\mathbf{M}_A\mathbf{R}_x\ddot{\theta}_x(x_A, y_A, t), \tag{15}$$

$$M_{ABHy} = -\mathbf{R}_y^T\mathbf{M}_A\ddot{\mathbf{w}}_A = -\mathbf{R}_y^T\mathbf{M}_A\boldsymbol{\phi}_A\ddot{\mathbf{q}}_A - \mathbf{R}_y^T\mathbf{M}_A\mathbf{R}_y\ddot{\theta}_y(x_A, y_A, t). \tag{16}$$

After the force F_{ABH} and the moments M_{ABHx} and M_{ABHy} are obtained, the two sets of ordinary differential equations, Eq. (5) and Eq. (9), are solved alternately in the time domain. As shown in Fig. 2, the fourth-order Runge-Kutta method is used to solve Eq. (5) to obtain the temporal function $q_n(\tau)$. Combining this with Eq. (4) gives the panel displacement, from which we get the ABH's installation-position acceleration. Substituting these accelerations into Eq. (12) yields the modal force $\mathbf{F}$. Then, using $\mathbf{F}$ in Eq. (9) gives the ABH's modal coordinates, and Eq. (7) is used to solve for the next-step force $\bar{F}^*_{ABH,n}$. This iterative process is repeated until the convergence criterion is met.

2.3. Verification and analysis

To validate the accuracy of the proposed coupled aeroelastic model and analyze the impact of ABH-induced modes, a representative panel-ABH configuration is constructed. The panel dimensions were set as $a = 500mm$, $b = 500mm$, with thickness $h = 1.33mm$ respectively, and its material properties are summarized in Table 1. The ABH structure is illustrated in Fig. 3. It features an asymmetric rectangular configuration with ABH characteristics. A damping layer, with a constant thickness h_d and width of d, is bonded along its edge. The ABH structure is segmented into three main parts: a central uniform rectangular platform with a constant thickness h_0 and size of $6mm \times 6mm$, four regions with varying thickness, and another platform of constant thickness h_1. The change function in the variable thickness region is described as follows:

$$h(x) = \varepsilon_i x^{2.5} + h_0, i = 1, 2, 3, 4 \tag{17}$$

where $\varepsilon_i = \frac{h_0 - h_1}{(d_i)^{2.5}}$.

The material parameters are detailed in Table 1, while the geometric parameters implemented in this study are outlined in Table 2.

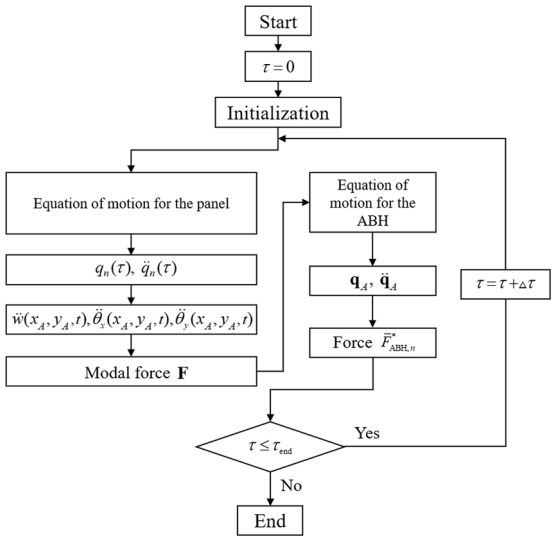

Fig. 2. Flowchart of iteration process.

Table 1
Structural material parameters.

Structures	Young's modulus (Pa)	Density (kg/m^3)	Poisson's ratio	Material loss factor
Panel	7.1×10^{10}	2710	0.346	0.001
ABH	9×10^9	2700	0.346	0.001
Damping	2×10^8	1800	0.45	0.3

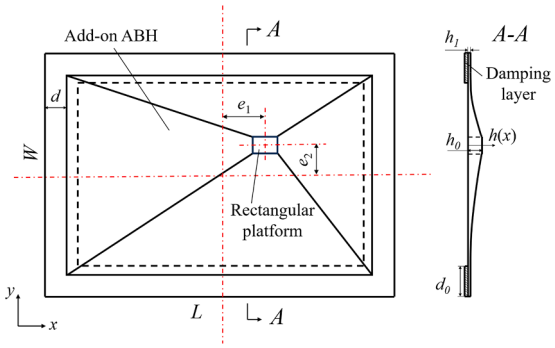

Fig. 3. Schematic of ABH structure.

The total mass of the ABH amounts to 0.0559 kg, which represents 6.21 % of the panel's mass (0.901 kg).

Numerical analysis of the ABH is carried out using the commercial software, Abaqus. The finite element model is shown in Fig. 4, which adopts C3D20R 3-D elements with 20 nodal points. The mesh of the ABH FEM model comprises 28,778 nodes and 4378 elements. A clamped boundary is applied at the panel–ABH interface.

The flow conditions follow standard assumptions for supersonic piston theory. Specifically, the flow–structure interaction is characterized by specific assumptions regarding the ratio $\mu/Ma = 0.1$, the in-plane external force $\bar{p}_x^{(a)} = \bar{p}_y^{(a)} = -\pi^2$, and a varying λ. Following the approach in Ref [20], the displacement of the panel is approximated using $M = 6$ assumed basis functions to ensure adequate accuracy while maintaining computational efficiency. In parallel, the ABH modal truncation number is denoted by L, representing the number of retained ABH structural modes. Drawing on the findings of Ref [20], which revealed a close correlation between the modal cutoff frequency of the ABH and the panel flutter frequency, with computational accuracy being guaranteed when the cutoff frequency is three times the critical flutter frequency. In this study, a more conservative criterion is applied, and the 20 lowest ABH modes including translational (z-direction) and rotational (x- and y-axis) components are retained, ensuring the modal cutoff frequency exceeds five times the flutter frequency, which is 52.2 Hz for the ABH with parameters shown in Tables 1 and 2. The corresponding modal frequencies, damping ratios, and participation factors[27] are listed in Table 3.

The ABH is installed at position $(0.65a, 0.5b)$ of panel, which is also selected as the monitoring point of response. The bifurcation curves of the panel response calculated using three different models under varying flow velocities are presented in Fig. 5. The model labeled "commercial software" is directly solved by constructing a fluid-structure interaction system using Ansys Workbench software [19]. The "Reduced Model" considers only the translational rigid-body displacement (in the z-direction) at the ABH-panel interface. This model employs von Karman theory and first-order piston theory to establish panel's governing equations and leveraging finite element method to derive a reduced discrete model of ABH, which are solved iteratively through the interaction forces [20]. The "Improved Model" shares the same calculation process as "Reduced Model", but additionally considers the degrees of freedom about the rotational with respect to the x-axis and y-axis at interface, which have been elaborated in Section 2.2. The vertical axis represents the dimensionless amplitude of the response w_p at the monitoring point when a stable limit cycle oscillation (LCO) is induced in panel.

Fig. 5 demonstrates that the dynamic pressure and the LCO amplitude predicted by the improved model matches the result of the finite-element-based fluid-structure coupling model better than the original model developed in the former study, thereby confirming the importance of including rotational Degrees of Freedom (DOFs) to improve accuracy. The result also indicates that the rotational degrees of freedom also play a certain role in flutter suppression, even though the contribution by the translational degrees of freedom is more significant in flutter suppression. The contribution of an ABH mode in flutter suppression depends on its modal participation factor, modal damping ratio and the degree of proximity between its frequency and flutter frequency. It is obvious that the translational participation factor of most modes in Table 3 is greater than the rotational ones. It means that the contribution of the

Table 2
Structural geometric parameters. (mm).

Parameter	d	d_0	e_1	e_2	h_0	h_1	h_d	L	W
Value	13	15	11	5	3	0.3	1	176	148

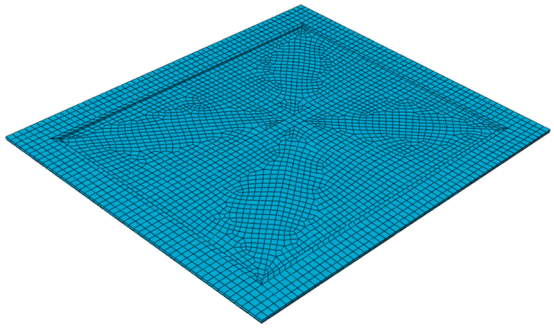

Fig. 4. Mesh of the ABH structure.

Table 3
The parameters of first 20 modes (ABH).

Modal order	Frequency (Hz)	Modal damping ratio	Modal participation factors $\alpha_i^{(1)}$	$\alpha_i^{(2)}$	$\alpha_i^{(3)}$
1	27.38	0.026	0.0870	0.0034	0.0078
2	29.84	0.030	0.0473	-0.0048	0.0048
3	35.36	0.030	0.0770	0.0049	-0.0031
4	39.60	0.030	0.0813	-0.0033	-0.0043
5	48.08	0.032	-0.0343	-0.0002	-0.0006
6	60.32	0.047	-0.0134	-0.0014	-0.0019
7	65.32	0.040	0.0006	-0.0036	0.0008
8	85.61	0.061	0.0803	-0.0002	0.0007
9	90.55	0.073	-0.0004	0.0004	-0.0003
10	112.11	0.067	0.0019	-0.0001	-0.0027
11	121.63	0.077	-0.0024	0.0016	-0.0002
12	139.05	0.071	0.0019	-0.0004	-0.0002
13	158.50	0.065	-0.0386	-0.0004	-0.0005
14	172.45	0.068	-0.0049	0.0011	-0.0002
15	190.17	0.055	-0.0406	-0.0002	-0.0020
16	215.06	0.079	-0.0190	-0.0001	-0.0004
17	220.62	0.060	-0.0226	-0.0001	0.0013
18	237.02	0.062	0.0001	0.0006	-0.0004
19	254.48	0.058	0.0310	0.0015	0.0002
20	263.89	0.060	0.0312	-0.0008	0.0001

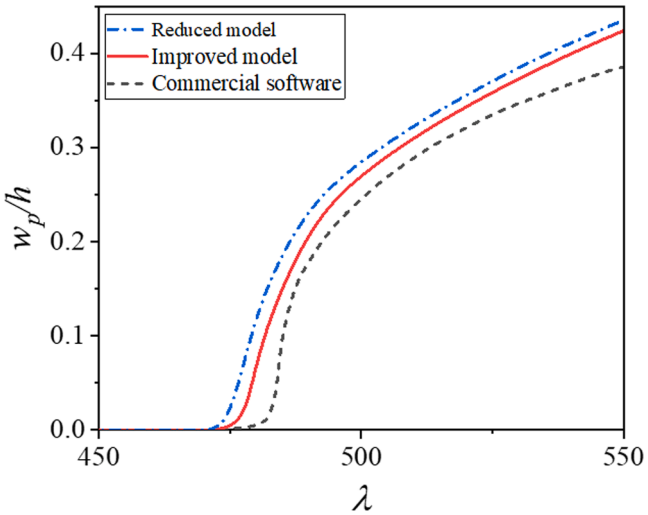

Fig. 5. Bifurcation diagrams of the aeroelastic responses under different calculation models.

translational motion is larger than the rotational motion in flutter suppression. This is also the reason why only the translational motion was considered in the previous studies.

To evaluate the effectiveness of different ABH modes in flutter suppression, a series of simulations are conducted using the modal condensation method, where specific modes are selectively excluded. Some of the results are shown in Fig. 6. Several key insights are summarized below:

1) The contribution of the modes with small modal participation factors, such as the 9th and 18th, are negligible in flutter suppression regardless of frequency proximity or damping level. This phenomenon is not difficult to understand because the modal participation factor is a metric of coupling characteristics between the ABH mode and the panel.
2) Some modes, like the 6th, have moderate participation factor, but have stronger effect the flutter boundary than the 15th, 19th, and 20th modes as shown in Fig. 6(a), indicating coupling strength is not determined by any single parameter. Because the flutter frequency of the panel is 52.2 Hz and the frequency becomes a little higher when the ABH is installed, the frequency of the 6th mode (60.32 Hz) is very close to the flutter frequency.
3) Although the 15th, 19th, and 20th modes exhibit large modal participation factors, they have little influence due to frequency mismatch with flutter, as shown in Fig. 6(a). The reason for this phenomenon is that the natural frequencies of these modes are far from the flutter frequency.
4) Although the 10th and 12th modes have similar z-directional modal participation factors, yet removing the 10th has a larger effect than removing the 12th mode, as shown in Fig. 6(b). This can be attributed to its significant participation in y-axis rotation.
5) In contrast, even though the 7th mode has notable x-axis rotational participation, its effect is negligible, as shown in Fig. 6(b). Since the ABH is installed in the midpoint in the y-direction, according to Eq. (7), the x-axis rotational motion of panel at this point is almost zero. It means that the rotational degree of freedom with respect to x-axis is always negligible regardless of the modal participation factors.

The above results indicates that effectiveness of an ABH mode in flutter suppression depends on many factors: its modal damping ratio, modal participation factors corresponding to different degrees of freedom, frequency proximity and installation position of the ABH. It is also obvious that inclusion of the rotational degrees of freedom in the interaction force in Eq. (3) can improve the accuracy of computation. The flutter suppression performance of an ABH will also depends on the total number of modes that can effectively suppress flutter. Moreover, the number of effective modes and the effectiveness of each mode depends on the parameters of the ABH.

In summary, the aeroelastic suppression performance is determined by the design parameters of the ABH structure and its installation position. To maximize the performance of flutter suppression, a simultaneous optimization of the ABH geometry parameters and its installation position on the panel is necessary. At each step in the iterative process of optimization, the aeroelastic response of the panel must be evaluated based on new geometry parameters of the ABH and its installation position. It means that the modes of the ABH will have different natural frequencies, different modal damping ratios and different modal participation factors. Hence, the simultaneous optimization process is computationally costly.

Therefore, to address the dual challenges of high computational cost and complex modal interaction, a data-driven optimization framework is adopted. This approach enables rapid evaluation and intelligent selection of effective ABH configurations by capturing the complex relationships between geometric parameters, modal behavior, and flutter response, thus providing a more practical and scalable solution for ABH design in aeroelastic applications.

2.4. The optimization problem for boosting flutter boundary

It has clarified in the previous section that the modal participation factors, natural frequencies, and damping ratios, and the

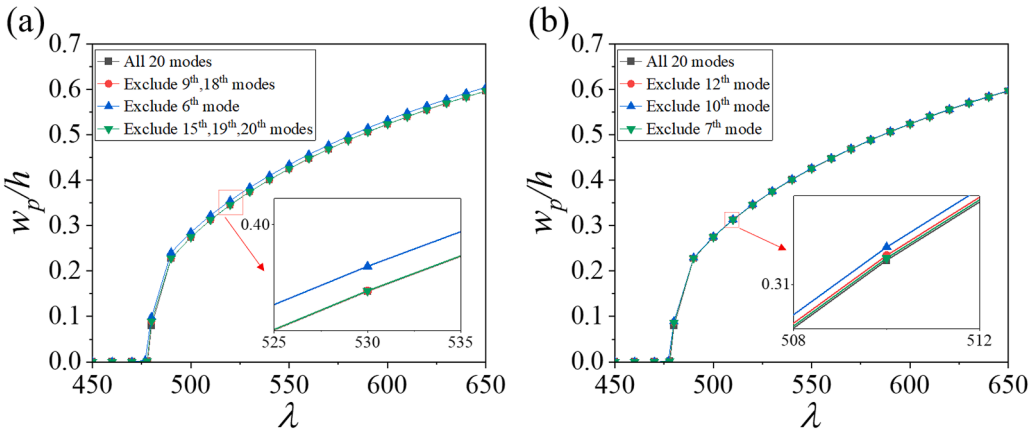

Fig. 6. The influence of different ABH modes on calculation. (a) 6th, 9th, 15th, 18th, 19th, 20th modes, (b) 7th, 10th, 12th modes.

installation position of the ABH affect the performance of aeroelastic flutter suppression of the panel. The modes with high modal participation factors, frequencies close to the flutter frequency, and significant damping ratios can effectively suppress panel flutter. The position of the ABH installation determines the coupling strength between the ABH structure and the host panel.

The modal characteristics of the ABH depends on its geometrical parameters. In order to illustrate how the geometrical parameters of the ABH and its installation position influence flutter boundary of the panel, the ABH shown in Fig. 4 is chosen as the baseline and the flutter boundary of panel is calculated when one of geometrical parameters and position parameter is changed. Fig. 7 illustrates how variations in several key geometric parameters, including the extension platform width d, rectangular platform eccentricity e_1, e_2, maximum length L and width W, and the chordwise installation position x_A, affect the flutter boundary. These results clearly demonstrate the complexity and nonlinearity of the relationships between structural parameters, installation position, and flutter suppression performance, indicating that traditional gradient-based optimization approaches are inadequate.

Furthermore, due to the intricate coupling among these parameters, the influence of altering any single parameter on flutter performance significantly depends on the specific values of the other parameters. Thus, the effectiveness of flutter suppression is not only a function of individual parameter settings but also of their interactions. This complex interdependency necessitates a comprehensive and systematic optimization approach rather than a single-factor analysis or empirical optimization.

Therefore, this is an optimization problem aimed at designing the geometric parameters of the ABH structure and its installation position to enhance the flutter critical boundary. Obviously, the flutter boundary λ_f is an implicit function of the geometrical parameters of the ABH and its installation position, that is $\lambda_f = \lambda_f(\mathbf{x})$, where $\mathbf{x}$ is a vector consisting of the geometrical parameters of the ABH and the coordinate of its installation position, denote as $\mathbf{x} = \{d, e_1, e_2, L, W, x_A\}$. The mass of the ABH is also a function of the geometric parameters, and can also be expressed as $m_A = m_A(\mathbf{x})$. A constraint of maximum mass is also imposed: $m_A \le m_{A\max}$. Therefore, the optimization problem can be expressed as

$$\lambda_f = \max_{\mathbf{x}\in\bar{\mathbf{x}}} \lambda_f(\mathbf{x}) \quad \text{s.t.} \quad m_A(\mathbf{x}) \le m_{A\max}. \tag{18}$$

Since no explicit expression is available for the function $\lambda_f(\mathbf{x})$, and the computation of the flutter boundary for each given set of parameters is costly in computer resource. Hence a data-driven collaborative optimization method, as introduced in the next section, is used in this study.

3. Data-driven optimization

3.1. Overall optimization strategy

The proposed data-driven optimization strategy aims to efficiently tackle the complexities identified in Section 2.4, specifically the nonlinear and highly coupled interactions among ABH geometric parameters, installation positions, and the flutter critical boundary. The optimization framework, depicted in Fig. 8, follows a closed-loop iterative process with four core steps and a feedback mechanism:

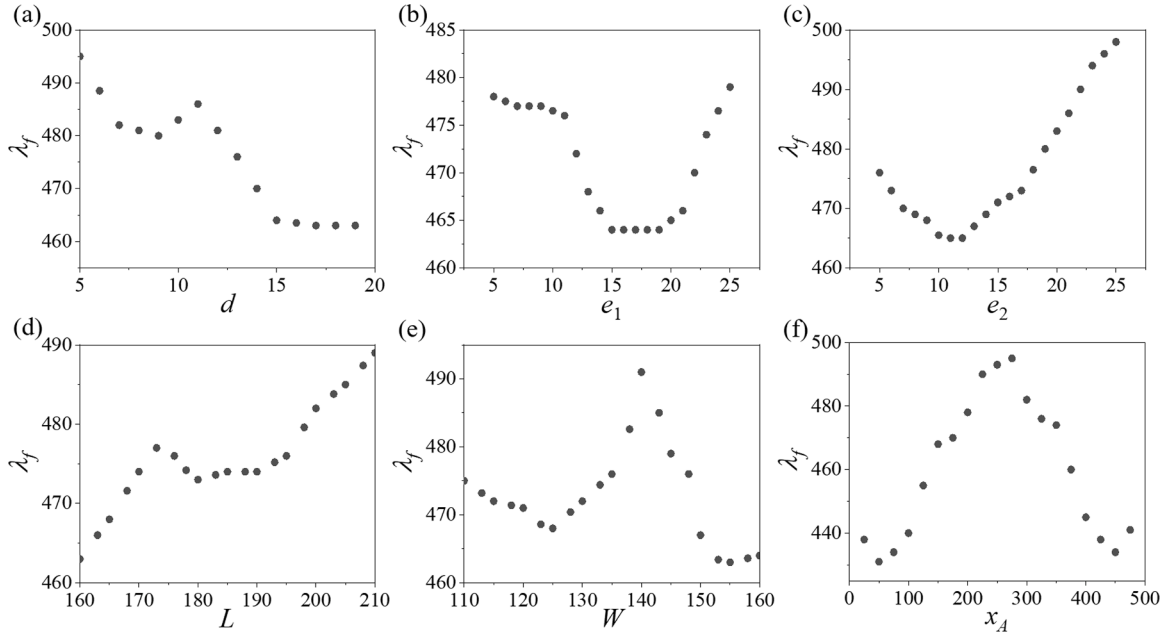

Fig. 7. The relationship between the geometric parameters and installation position of ABH and the critical flutter boundary. (a) Geometric parameter d, (b) geometric parameter e_1, (c) geometric parameter e_2, (d) geometric parameter L, (e) geometric parameter W, (f) installation position x_A.

data initialization (Step 1), surrogate model building (Step 2), GA optimization (Step 3), and convergence criteria (Step 4). In Step 1, based on the improved model, data points are generated and simulated to form a preliminary dataset. Step 2 involves using the initialized dataset to train a surrogate model, which is used to approximate complex physical simulations. In Step 3, the GA leverages the surrogate model to iteratively search for improved designs and generate new optimal solutions. Finally, in Step 4, it is checked whether the optimized solution meets the requirements. If not, the feedback loop is activated and the surrogate model is retrained (returning to Step 2). Once satisfied, the optimal ABH design is output.

3.2. Data initialization

In this step, Latin Hypercube Sampling [28,29] is employed due to its effectiveness in uniformly sampling the parameter space. The sampled data points $N_{initial}$ are constrained by predefined lower and upper bounds $\mathbf{x}_{\min}$ and $\mathbf{x}_{\max}$, resulting in an initial dataset comprising samples. These samples are evaluated using the improved aeroelastic model described in Section 2.2 and finite element simulations, producing corresponding flutter boundary values $\lambda_f = \{\lambda_f(\mathbf{x}_1), \lambda_f(\mathbf{x}_2), \cdots \lambda_f(\mathbf{x}_{N_{initial}})\}$. This procedure generates an initial database $\mathbf{D}_{total}$, as shown in Fig. 9.

3.3. Surrogate model building

In this step, a surrogate model is adopted to approximate the relationship between ABH parameters and flutter performance, thereby expediting optimization. Fig. 10 outlines the surrogate modeling process, utilizing a GA-BP neural network to enhance predictive accuracy and computational efficiency, as detailed in Fig. 11.

Specifically, the neural network architecture comprises an input layer corresponding to ABH parameters, two hidden layers designed for feature extraction-containing 4 neurons in the first hidden layer and 2 neurons in the second-and an output layer representing flutter boundary predictions. The Rectified Linear Unit activation function is employed in hidden layers [30], chosen for its effectiveness in modeling nonlinear relationships and computational efficiency. The initial dataset $\mathbf{D}_{total}$, consisting of $N_{initial}$ data points, is partitioned such that the first 10 data points form the independent test set, denoted as $\mathbf{D}_{test}$, and the remaining data points constitute the training set, denoted as $\mathbf{D}_{trian}$. This partition ensures the surrogate model's predictive accuracy and robustness. The GA optimizes network weights by minimizing prediction errors (real error, RE) defined as:

$$RE = \frac{\| \lambda_f - \widetilde{\lambda}_f \|_2}{\| \lambda_f \|_2} \tag{19}$$

where, λ_f the real results, and $\widetilde{\lambda}_f$ the prediction results.

This iterative optimization continues until the surrogate model achieves satisfactory accuracy IS_1 on the test dataset, thus ensuring its reliability for subsequent optimization tasks.

3.4. GA optimization

As illustrated in Fig. 12, GA optimization can leverage this surrogate model to iteratively explore and refine ABH parameter sets. The initial dataset $\mathbf{D}_{total}$ serves as the GA's initial population, with the fitness function defined explicitly to maximize flutter boundary values. The GA incorporates genetic operations such as crossover and mutation, evolving the population toward optimal solutions. When the flutter critical boundary reaches its maximum, the corresponding geometric parameter vector is recorded. Given that

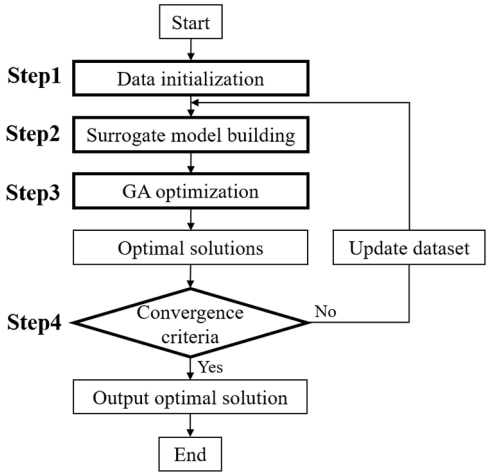

Fig. 8. Schematic diagram of overall optimization strategy.

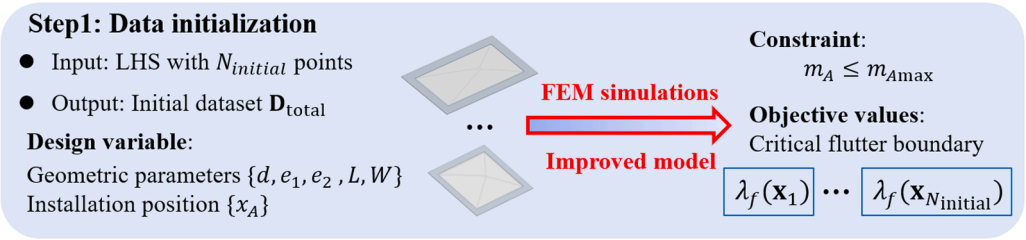

Fig. 9. Schematic diagram of the data initialization process.

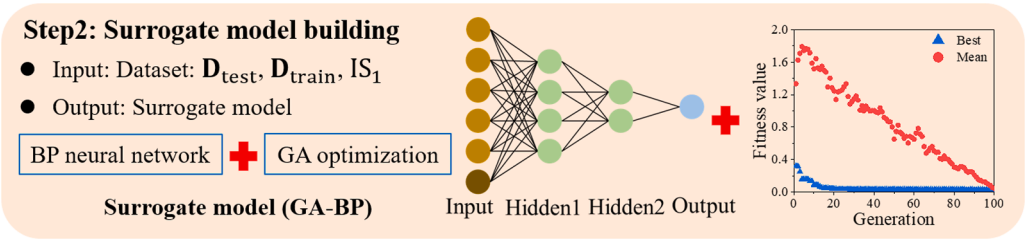

Fig. 10. Schematic diagram of the surrogate model building process.

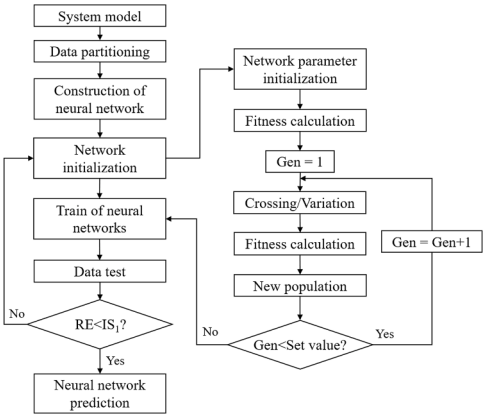

Fig. 11. Flowchart of the GA-BP surrogate model.

multiple geometric parameter combinations might yield similarly optimal flutter boundary values, several sets of optimal parameters are selected as candidate solutions in each iteration, where the number of new ABH designs denoted as N_S. These parameter sets are subsequently evaluated using the improved aeroelastic model to obtain their true flutter boundary values, after which the dataset $\mathbf{D}_{total}$ and the training set $\mathbf{D}_{trian}$ are updated accordingly.

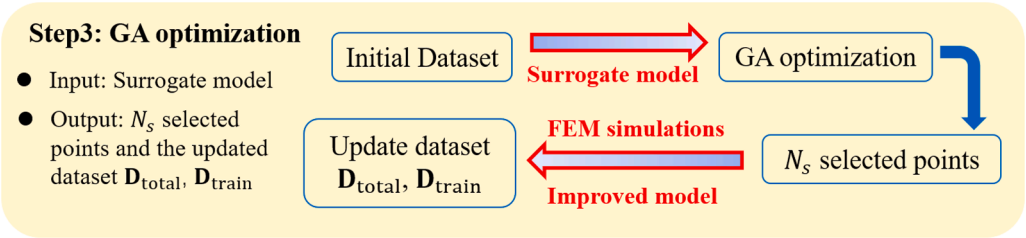

Fig. 12. Schematic diagram of the surrogate data-driven optimization process.

3.5. Convergence criteria

The optimization process employs a convergence criterion based on the root mean square error (RMSE) between surrogate model predictions and actual simulation results for newly generated candidate solutions. As shown in Fig. 13, RMSE is defined by:

$$RMSE = \sqrt{\frac{\sum_{i=1}^{N_S}\left(\lambda_f(\mathbf{x}_i) - \widetilde{\lambda}_f(\mathbf{x}_i)\right)^2}{N_S}} \tag{20}$$

To determine whether convergence is achieved, the calculated RMSE is compared against a predefined convergence threshold. When the RMSE falls below IS_2, the surrogate model is considered sufficiently accurate, and the optimization process is terminated. Otherwise, the iterative process continues with further data augmentation and retraining of the surrogate model. This comparison with IS_2 ensures that only when the prediction error is acceptably low, the resulting ABH design is accepted as optimal. Through this iterative refinement, the process guarantees both reliability and efficiency in identifying robust ABH configurations for enhanced flutter suppression performance.

4. Results and discussion

4.1. Calculation and convergence

The geometrical parameters of the ABH and its installation position are optimized based on the above method. Specifically, the lower bound is set empirically to $\mathbf{x}_{\min} = \{5, 5, 5, 160, 110, 50\}$ and the upper bound to $\mathbf{x}_{\max} = \{20,25,25,210,160,450\}$. The constraint of maximum mass is imposed $m_{Amax} = 0.065kg$. The initial number of data points $N_{initial}$ is set to 40, with the first 10 data points in dataset $\mathbf{D}_{total}$ designated as the test dataset $\mathbf{D}_{test}$ and the remaining data points as the training dataset $\mathbf{D}_{trian}$. In Step 2, IS_1 is set to 0.04, with a population size of 100, 100 generations of iterations, the crossing probability of 0.8, and the variation probability of 0.1. In Step 3, GA's population size is set to 100, with 700 generations of iterations, the crossing probability of 0.8, and the variation probability of 0.1. The number of new ABH designs N_S, is set to 5. In Step 4, IS_2 is set to 0.02.

The final surrogate model and optimization results were obtained after 37 iterations of computation. The prediction results for the test data $\mathbf{D}_{test}$ based on the surrogate model are shown in Fig. 14, with the RE value of 0.0124. These results indicate that the predictions from the surrogate model are largely consistent with the real results, demonstrating the reliability of the model. The relationship between the RMSE value obtained after each iteration of Steps 2, 3, and 4 and the iteration times is illustrated in Fig. 15, with the RMSE value of 0.01899, indicating the reliability of the optimization results. From the five sets of ABH geometric parameters obtained after the final iteration of the data-driven optimization method, one specific set is selected to demonstrate the suppression effect of the optimized ABH structure on panel flutter. The geometric parameters of the ABH are $\mathbf{x}_{optimal} = \{7,24,7,206,120,305\}$, with the corresponding flutter critical boundaries being $\lambda_f = 568$.

The geometrical parameters of the baseline ABH and optimized ABH are shown in Table 4 for comparison. It is obvious that the optimized ABH is longer in the streamwise direction and shorter in the spanwise direction than the baseline ABH. The width of the extension platform d becomes smaller, but both the eccentricities e_1 in the streamwise direction and e_2 in the spanwise direction become greater.

4.2. Discussions

The optimized ABH structure has a mass of 0.0571 kg, accounting for approximately 6.33 % of the panel mass, which satisfies the mass constraint and is comparable to the case study structure. Meanwhile, the installation position has been optimized, which better conforms to the influence law shown in Fig. 7(f) and can improve the flutter critical boundary of the panel more effectively. Table 5. lists the modal parameters of the first 20 modes. Based on the improved modeling approach that incorporates rotational DOFs, the bifurcation diagram of the panel's aeroelastic response was recalculated, as shown in Fig. 16.

Compared with the baseline case, the optimized ABH significantly elevates the flutter critical boundary from 439 to 568, achieving a 29.4 % improvement in flutter suppression. Given that the performance is governed by modal characteristics, further analysis is conducted in terms of effective modal distribution and modal effective mass to elucidate the underlying mechanisms.

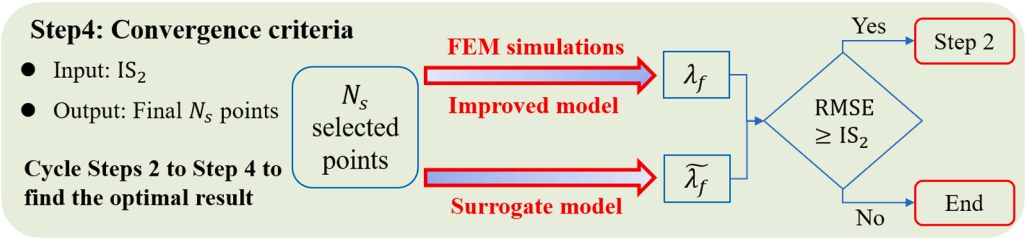

Fig. 13. Schematic diagram of the surrogate result judgment process.

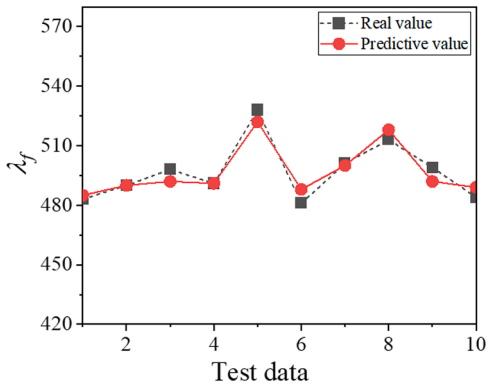

Fig. 14. The flutter critical boundaries of test data.

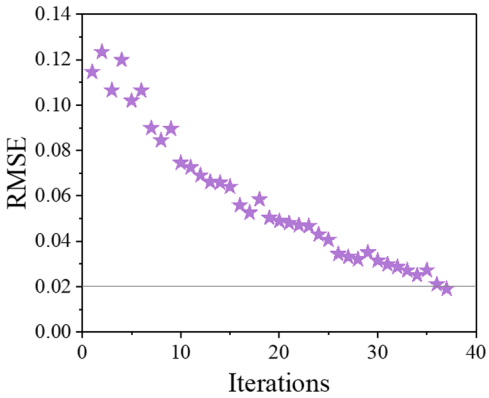

Fig. 15. The relationship between the RMSE and iterations.

Table 4
Comparison of design parameters for two ABHs. (mm).

Parameter	d	e_1	e_2	L	W	x_A
ABH (baseline)	13	11	5	176	148	325
ABH (optimized)	7	24	7	206	120	305

a) Higher modal density of ABH around the flutter frequency

As introduced in the former study, the ABH installed on the panel functions as a linear energy sink, which is realized by the interaction between is the modes of the ABH and the panel. The effective of energy extraction by the ABH depends on modal damping ratio, frequency proximity and coupling strength. Therefore, it is important for the ABH to have more high-damping coupled modes near the flutter frequency. Fig. 17 shows the modal damping ratios of the three structures: the panel, the original ABH configuration, and the optimized ABH design. The damping ratio of the panel is relatively low and its first and second natural frequencies are 46.74 Hz and 95.32 Hz, respectively.

It is well known that the panel flutter motion is a combination of the first and second modes of the panel and its flutter frequency varies between the two natural frequencies, depending on the dynamic pressure parameter λ. Fig. 18 presents the pure panel's normalized aeroelastic response spectra at different λ values. As λ increases, the peak response frequency gradually shifts higher but remains between the first and second natural frequencies of the panel, indicating that the flutter response is dominated by a coupling of these two modes.

Within this critical frequency range, the original ABH design introduces four modes (the 5th, 6th, 7th, and 8th), while the optimized ABH introduces six modes (the 3rd through 8th), with more uniform spacing. This expanded and more evenly distributed modal set improves the likelihood of frequency matching and spatial overlap with the panel's dominant flutter modes, enhancing the ABH-panel coupling efficiency. Despite the improved flutter performance, the modal damping ratios of the ABH modes remain similar between the original and optimized designs. This is because both use the same damping material and exhibit comparable geometric taper profiles, resulting in equivalent energy dissipation characteristics. The improvement stems from the redistribution and alignment of modal

Table 5
The parameters of first 20 modes (optimized ABH).

Modal order	Frequency (Hz)	Modal damping ratio	Modal participation factor $\alpha_i^{(1)}$	$\alpha_i^{(2)}$	$\alpha_i^{(3)}$
1	22.48	0.023	0.1060	0.0014	0.0114
2	29.41	0.036	0.0118	-0.0045	0.0015
3	45.87	0.027	0.0715	0.0034	-0.0044
4	53.28	0.029	0.0565	-0.0026	-0.0043
5	61.70	0.049	0.0689	0.0011	0.0025
6	78.85	0.037	-0.0296	-0.0034	-0.0002
7	84.80	0.047	-0.0055	0.0015	0.0007
8	96.33	0.041	-0.0776	0.0007	-0.0037
9	107.78	0.052	0.0370	0.0019	-0.0003
10	129.74	0.040	0.0388	-0.0018	-0.0001
11	147.10	0.066	-0.0468	0.0006	0.0013
12	155.72	0.057	0.0321	0.0006	-0.0004
13	167.18	0.065	0.0014	-0.0004	0.0002
14	186.29	0.060	0.0434	-0.0002	0.0020
15	197.32	0.074	0.0024	0.0001	0.0002
16	214.43	0.063	-0.0029	0.0009	0.0005
17	233.09	0.065	-0.0358	-0.0004	0.0000
18	269.63	0.001	-0.0140	0.0000	0.0000
19	271.63	0.051	0.0122	0.0002	-0.0010
20	282.25	0.051	-0.0011	-0.0009	0.0000

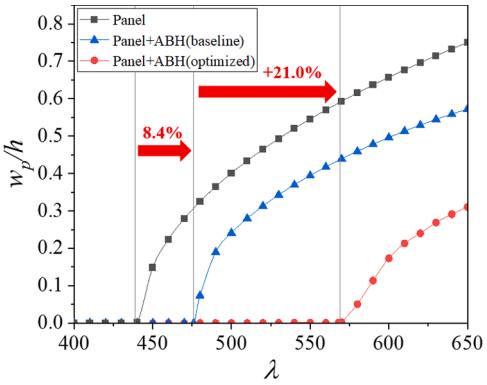

Fig. 16. The bifurcation diagrams for aeroelastic response of different panel configurations.

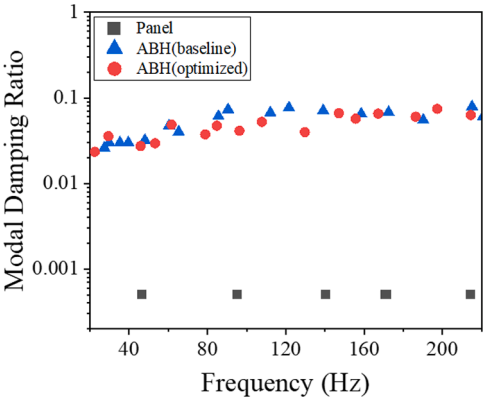

Fig. 17. Modal damping ratio of different structures.

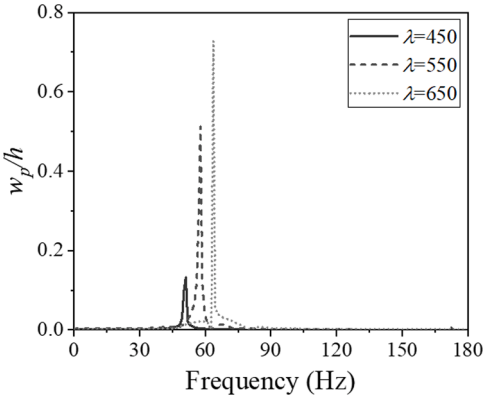

Fig. 18. Frequency translation with λ changed.

frequencies within the flutter-relevant range, rather than from changes in damping capacity.

b) Effective modal mass

As shown above, the coupling strength is an important factor for the ABH to extract energy from the host structure. On the other hand, the coupling strength is measured by the coupling coefficient, consisting of two parts, one is directly related to the effective modal mass and the other is related to the installation position [17]. As shown in the beginning of this section, the installation was optimized. Hence, it is important to further examine the variation of effective modal mass after optimization.

The modal participation factors $\alpha_i^{(k)}(k=1,2,3)$ of baseline ABH are shown in Table 3 and those of the optimized ABH are shown in Table 5 [27]. the effective modal mass $m_i^{(k)} = \left(\alpha_i^{(k)}\right)^2 (k=1,2,3)$ is the square of the modal participation factor under the premise of modal mass normalization. And the cumulative effective modal mass proportion (CEMMP) is used to quantify how much of the structural response is captured by the low-order modes in each direction. The CEMMP of the first L - order modes given is defined as follows:

$$CEMMP = \frac{\sum_{i=1}^{L} m_i^{(k)}}{\sum_{i=1}^{\infty} m_i^{(k)}}, (k=1,2,3) \tag{21}$$

where the denominators correspond to the mass of the ABH structure and the moments of inertia about the x- and y-axis when $k = 1,2,3$, respectively.

Fig. 19 compares the CEMMP curves of the original baseline ABH and optimized ABH in the z-axis translation, as well as for rotational motion about the x- and y- axis. After optimization, the CEMMP increases in the z-axis translation and y-axis rotation, while it decreases in x-axis rotation. This kind of variation in CEMMP before and after optimization is reasonable if the installation position of the ABH is taken into consideration. Since the ABH is installed in the centerline in the spanwise direction and the displacement of the panel is symmetrical with respect to this centerline, there is no rotational motion with respect to the centerline.

This result can also be explained by Eq. (7). At the centerline in the spanwise direction, $\eta_A = 1/2$ and the second term on the right-hand side of Eq. (7) is zero. Hence, $\overline{M}_{\mathrm{ABH}x}$ has no contribution to the force $\overline{F}^*_{ABH,n}$ for all n. That is, the rotational motion of the ABH with respect to the x-axis is not coupled with the panel so that the CEMMP in x-axis rotation does not affect flutter response of the panel. The z-direction and y-rotation components contribute effectively to flutter suppression because ABH-induced forces in these directions can strongly couple with panel deformation and dissipate energy.

This trend confirms the physical correctness of the optimization: modal mass is concentrated in the directions that offer meaningful resistance to aeroelastic excitation. It also validates the necessity of including y-rotational degrees of freedom in the modeling process. While the z-direction generally dominates due to larger participation factors and effective mass, the contribution from y-rotation is non-negligible and cannot be ignored. This provides further support for the improved model developed in this work, which extends previous reduced-order approaches that considered only z-directional motion.

5. Conclusions

This study proposes an optimization framework for improving the aeroelastic performance of panel with ABH, integrating data-driven methods with physical mechanism-based modeling to achieve both accuracy and efficiency.

A key contribution is the development of a multi-dimensional reduced-order coupling model that incorporates not only the conventional z-directional motion but also rotational DOFs around the x- and y- axis. While previous studies often neglected rotational

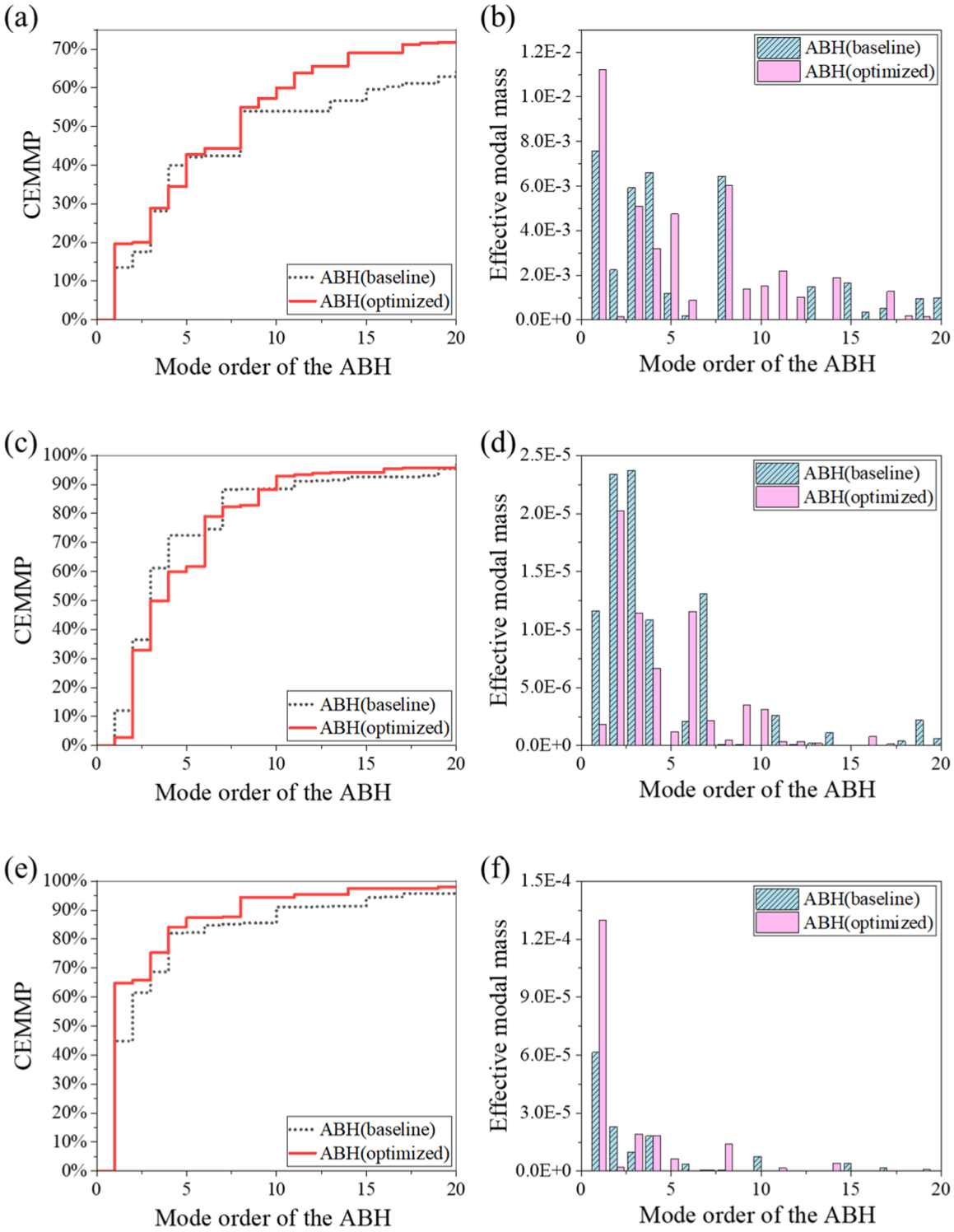

Fig. 19. CEMMP and effective modal mass results of two ABH structures. (a) CEMMP in *z*-direction, (b) effective modal mass in *z*-direction, (c) CEMMP in *x*-rotational direction, (d) effective modal mass in *x*-rotational direction, (e) CEMMP in *y*-rotational direction, (f) effective modal mass in *y*-rotational direction.

components due to their relatively small modal contributions, the results of this study demonstrate that including these rotational DOFs significantly improves the accuracy of interaction force predictions. Although the z-direction remains dominant owing to its larger modal participation and effective mass, rotational effects are shown to be non-negligible and must be accounted for in the modeling process.

To address the computational burden of conventional optimization, a surrogate modeling approach combining a GA-BP neural network is employed. This strategy significantly reduces the number of required finite element simulations while maintaining high accuracy through iterative validation against finite element results. The optimized ABH configuration can enhance the panel's flutter boundary by up to 29.4 %, nearly tripling the initial effect, confirming the effectiveness of the approach and the physical soundness of the optimized solution.

CRediT authorship contribution statement

Zhuogeng Zhang: Writing – original draft, Formal analysis, Data curation, Conceptualization. **Xiaodong Wang:** Writing – review & editing, Methodology. **Hongli Ji:** Writing – review & editing, Visualization, Investigation, Funding acquisition, Formal analysis. **Jinhao Qiu:** Supervision, Project administration, Methodology, Funding acquisition. **Li Cheng:** Supervision, Methodology.

Declaration of competing interest

The authors declare that they have no known competing financial interests or personal relationships that could have appeared to influence the work reported in this paper.

Acknowledgements

This work is partially supported by the the National Natural Science Foundation of China (No. U2436204 & 52241103), and the Fundamental Research Funds for the Central Universities (NE2024002 & NP2024112). The work was also partially supported by grants from the RIAIoT (Research Institute for Artificial Intelligence of Things) through project P0049625.

Data availability

The data that has been used is confidential.

References

[1] S. Amirzadegan, S.M. Mousavi Safavi, A. Jafarzade, Supersonic panel flutter analysis assuming effects of initial structural stresses, J. Inst. Eng. India, Ser. C 100 (2019) 833–839, https://doi.org/10.1007/s40032-019-00532-y.
[2] N. Sharma, S. Mohapatra, E.K. Kumar, S.K. Panda, Geometrically nonlinear aeroelastic flutter characteristic of laminated composite shell panels under supersonic flow, Int. J. Appl. Mech. 15 (2023), https://doi.org/10.1142/S1758825123500291.
[3] L. Ye, Z. Ye, K. Ye, J. Wu, Aeroelastic stability analysis of a flexible panel subjected to an oblique shock based on an analytical model, Acta Mech. 232 (2021) 3539–3564, https://doi.org/10.1007/s00707-021-03023-3.
[4] E. Verstraelen, G. Habib, G. Kerschen, G. Dimitriadis, Experimental passive flutter suppression using a linear tuned vibration absorber, AIAA J. 55 (2017) 1707–1722, https://doi.org/10.2514/1.J055397.
[5] D.R.Q. Pacheco, F.D. Marques, A.J.M. Ferreira, Panel flutter suppression with nonlinear energy sinks: numerical modeling and analysis, Int. J. Non-Linear Mech. 106 (2018) 108–114, https://doi.org/10.1016/j.ijnonlinmec.2018.08.009.
[6] J. Zhou, M. Xu, Z. Yang, Y. Gu, Suppressing nonlinear aeroelastic response of laminated composite panels in supersonic airflows using a nonlinear energy sink, Chin. J. Aeronaut 34 (2021) 376–385, https://doi.org/10.1016/j.cja.2020.09.012.
[7] J. Zhou, M. Xu, Z. Yang, Y. Gu, Suppression of panel flutter response in supersonic airflow using a nonlinear vibration absorber, Int. J. Non-Linear Mech. 133 (2021) 103714, https://doi.org/10.1016/j.ijnonlinmec.2021.103714.
[8] C.Y. Lee, J.H. Kim, Active flutter suppression of smart-skin antenna structures with piezoelectric sensors and actuators, Aerospace 8 (2021), https://doi.org/10.3390/aerospace8090257.
[9] C. Shao, D. Cao, Y. Xu, H. Zhao, Flutter and thermal buckling analysis for composite laminated panel embedded with shape memory alloy wires in supersonic flow, Int. J. Aeros p. Eng. 2016 (2016) 1–12, https://doi.org/10.1155/2016/8562716.
[10] Z.G. Song, T.Z. Yang, F.M. Li, E. Carrera, P. Hagedorn, A method of panel flutter suppression and elimination for aeroelastic structures in supersonic airflow, J. Vib. Acoust. 140 (2018), https://doi.org/10.1115/1.4039724.
[11] D.D. Bueno, C.G. Gonsalez Bueno, E.H. Dowell, A modal approach for designing controllers for active flutter suppression, J. Braz. Soc. Mech. Sci. Eng. 43 (2021), https://doi.org/10.1007/s40430-020-02754-z.
[12] C.A. McCormick, M.R. Shepherd, Design optimization and performance comparison of three styles of one-dimensional acoustic black hole vibration absorbers, J. Sound Vib. 470 (2020) 115164, https://doi.org/10.1016/j.jsv.2019.115164.
[13] W. Huang, H. Ji, J. Qiu, L. Cheng, Wave energy focalization in a plate with imperfect two-dimensional acoustic black hole indentation, J. Vib. Acoust. 138 (2016) 061004, https://doi.org/10.1115/1.4034080.
[14] E.P. Bowyer, V.V. Krylov, Experimental investigation of damping flexural vibrations in glass fibre composite plates containing one- and two-dimensional acoustic black holes, Compos. Struct. 107 (2014) 406–415, https://doi.org/10.1016/j.compstruct.2013.08.011.
[15] T. Zhou, L. Cheng, A resonant beam damper tailored with Acoustic Black hole features for broadband vibration reduction, J. Sound Vib. 430 (2018) 174–184, https://doi.org/10.1016/j.jsv.2018.05.047.
[16] H. Ji, N. Wang, C. Zhang, X. Wang, L. Cheng, J. Qiu, A vibration absorber based on two-dimensional acoustic black holes, J. Sound Vib. 500 (2021) 116024, https://doi.org/10.1016/j.jsv.2021.116024.
[17] H. Ji, X. Zhao, N. Wang, W. Huang, J. Qiu, L. Cheng, A circular eccentric vibration absorber with circumferentially graded acoustic black hole features, J. Vib. Acoust. (2022) 144, https://doi.org/10.1115/1.4053475.
[18] S. Park, J.Y. Lee, W. Jeon, Vibration damping of plates using waveguide absorbers based on spiral acoustic black holes, J. Sound Vib. 521 (2022) 116685, https://doi.org/10.1016/j.jsv.2021.116685.

[19] Z. Zhang, H. Ji, C. Tao, J. Qiu, L. Cheng, Suppression of panel flutter in supersonic flow based on acoustic black hole as a linear energy sink, J. Sound Vib. 571 (2024), https://doi.org/10.1016/j.jsv.2023.118030.
[20] Z. Zhang, H. Ji, J. Qiu, K. Yuan, L. Cheng, Coupled aeroelastic analysis of a panel in supersonic flow with add-on acoustic black hole, Chin. J. Aeronaut. 38 (2025), https://doi.org/10.1016/j.cja.2024.103390.
[21] J. Naranjo-Pérez, M. Infantes, J.Fernando Jiménez-Alonso, A. Sáez, A collaborative machine learning-optimization algorithm to improve the finite element model updating of civil engineering structures, Eng. Struct. 225 (2020), https://doi.org/10.1016/j.engstruct.2020.111327.
[22] I.G.A.G. Angga, M. Bellout, P.E.S. Bergmo, P.A. Slotte, C.F. Berg, Collaborative optimization by shared objective function data, Array 16 (2022), https://doi.org/10.1016/j.array.2022.100249.
[23] M.A. Bessa, S. Pellegrino, Design of ultra-thin shell structures in the stochastic post-buckling range using bayesian machine learning and optimization, J. Solids Struct. 139-140 (2018) 174–188, https://doi.org/10.1016/j.ijsolstr.2018.01.035.
[24] F. Liu, X. Jiang, X. Wang, L. Wang, Machine learning-based design and optimization of curved beams for multistable structures and metamaterials, Extreme Mech. Lett. 41 (2020), https://doi.org/10.1016/j.eml.2020.101002.
[25] J.K. Wilt, C. Yang, G.X. Gu, Accelerating auxetic metamaterial design with deep learning, Adv. Eng. Mater. 22 (2020), https://doi.org/10.1002/adem.201901266.
[26] E.H. Dowell, Nonlinear oscillations of a fluttering plate. I, AIAA J 4 (1966) 1267–1275, https://doi.org/10.2514/3.3658.
[27] J. Wijker, Spacecraft Structures, Springer-Verlag, Heidelberg/Berlin,Germany, 2008.
[28] J.P. Sun, G.J. Lv, X.G. Ma, An improved typhoon simulation method based on Latin hypercube sampling method, Sci. Rep. 12 (2022), https://doi.org/10.1038/s41598-022-13151-y.
[29] R. Sheikholeslami, S. Razavi, Progressive Latin Hypercube sampling: an efficient approach for robust sampling-based analysis of environmental models, Environ. Modell. Softw. 93 (2017) 109–126, https://doi.org/10.1016/j.envsoft.2017.03.010.
[30] Y.W. Xuan Qi, Xue Mei, Ryad Chellali, Shipin Yang, Comparative analysis of the linear regions in ReLU and LeakyReLU networks, in: ICONIP 2023. Communications in Computer and Information Science, Springer, Singapore, 2024.